Liu, Qing; Zhou, Yu; Shaukat, Ahmed; Meng, Zhuojun; Kyllönen, Daniella; Seitz, Iris;
Langerreiter, Daniel; Kuntze, Kim; Priimagi, Arri; Zheng, Lifei; Kostiainen, Mauri A.

Optically Controlled Construction of Three-Dimensional Protein Arrays

Please cite the original version:
Liu, Q., Zhou, Y., Shaukat, A., Meng, Z., Kyllönen, D., Seitz, I., Langerreiter, D., Kuntze, K., Priimagi, A., Zheng,
L., & Kostiainen, M. A. (2023). Optically Controlled Construction of Three-Dimensional Protein Arrays.
Angewandte Chemie - International Edition, *62*(28), Article e202303880. https://doi.org/10.1002/anie.202303880

Nanostructures

Optically Controlled Construction of Three-Dimensional Protein Arrays

Qing Liu, Yu Zhou, Ahmed Shaukat, Zhuojun Meng, Daniella Kyllönen, Iris Seitz,
Daniel Langerreiter, Kim Kuntze, Arri Priimagi, Lifei Zheng,* and Mauri A. Kostiainen*

Abstract: Protein crystallization is an important tool for structural biology and nanostructure preparation. Here, we report on kinetic pathway-dependent protein crystals that are controlled by light. Photo-responsive crystallites are obtained by complexing the model proteins with cationic azobenzene dyes. The crystalline state is readily switched to a dispersed phase under ultraviolet light and restored by subsequent visible-light illumination. The switching can be reversibly repeated for multiple cycles without noticeable structure deterioration. Importantly, the photo-treatment not only significantly increases the crystallinity, but creates crystallites at conditions where no ordered lattices are observed upon directly mixing the components. Further control over the azobenzene isomerization kinetics produces protein single crystals of up to $\approx 50\,\mu m$. This approach offers an intriguing method to fabricate metamaterials and study optically controlled crystallization.

Introduction

Bottom-up construction of hierarchically ordered structures offers a robust tool for fabricating nanomaterials. Mimicking natural structures and functions can provide an understanding of complex biological systems.[1] Proteins present an attractive building block to fulfill this task owing to their unparalleled properties. For example, the large compositional library (20 amino acids) creates abundant polypeptide sequences which can further fold into discrete protein structures.[1d] Many proteins display intrinsic structural symmetries, which favor structures with long-range periodicity.[2] Moreover, selected proteins (e.g. virus capsids) are compatible with noncognate payloads, such as nanoparticles,[3] self-assembled systems[4] and polymers,[5] leading to the formation of hybrid assemblies bearing unprecedented e.g. optical[7] and catalytic[6] properties. By using computational methods and recombinant techniques, *de novo* designed proteins and their assemblies can be engineered to further broaden this toolbox.[1d]

Diverse interactions are utilized as the driving force for protein assemblies. For example, with careful design and genetic engineering, amino acid residues at desired sites are substituted with coordinating ligands, and the subsequent addition of metal ions directs the formation of cage-like structures,[7] two-dimensional (2D) arrays,[8] or three-dimensional (3D) lattices.[9] With this approach, stimulus-responsiveness is realized, and other modules can also be incorporated, affording protein crystallization that is mediated by hydrophobic interactions[10] or disulfide bonds.[11] Most protein cages display a negatively charged exterior.[1b] Therefore, protein assemblies can be feasibly obtained by complexation with polycations via electrostatic interactions. However, taking advantage of the strong attractive forces mostly produces amorphous aggregates.[12] In order to avoid kinetically trapped assemblies and afford crystalline structures, the interaction strength needs to be adjusted to a weakly attractive regime by the addition of an electrolyte.[13] Therefore, introducing other easy-to-handle triggers to tune the assembly conditions would offer interesting approaches to preparing well-ordered and responsive protein assemblies.

Light is a non-invasive stimulus that can be delivered to closed systems with high temporal and spatial accuracy.[1a] Moreover, light-controlled assemblies omit the supply of molecular input and consequently the generation of molecular waste, which is of particular interest for the preparation of dissipative assemblies where the removal of waste is essential.[14] Due to these features, (crystalline) assemblies that can be controlled by light are gaining increasing attention, and they can be prepared by functionalizing the building block surface with light-sensitive ligands or introducing a photo-switchable medium.[1a] Recent advances highlight the second approach because it circumvents laborious preparation procedures and possible adverse

[*] Q. Liu, Z. Meng, Prof. L. Zheng
Wenzhou Institute, University of Chinese Academy of Sciences
Wenzhou 325001 (China)
E-mail: zhenglf@ucas.ac.cn

Q. Liu, Y. Zhou, A. Shaukat, D. Kyllönen, I. Seitz, D. Langerreiter,
Prof. M. A. Kostiainen
Biohybrid Materials, Department of Bioproducts and Biosystems,
Aalto University
02150 Espoo (Finland)
E-mail: mauri.kostiainen@aalto.fi

K. Kuntze, Prof. A. Priimagi
Smart Photonic Materials, Faculty of Engineering and Natural
Sciences, Tampere University
P.O. Box 541, 33101 Tampere (Finland)

effects on switching performance.[15] Particularly, controlling the photo-isomerization kinetics of the light-responsive modules can produce novel structures that are inaccessible by directly complexing the building blocks, such as 2D colloidal crystals[15j] and DNA fibres.[15g] However, the use of this strategy in the context of assembling 3D arrays and crystals remains elusive.[1a]

In this work, we report the pathway-dependent crystalline assembly of two model proteins (ferritin cages and tobacco mosaic virus, TMV) by using cationic azobenzene. One key feature of the system is the control over the assembly process by taking advantage of the isomerization kinetics of the photo-responsive molecules. Direct complexation of proteins with the azobenzene in the *trans*-state leads to the formation of crystallites with small ordered domains, which can be disassembled under UV irradiation due to the *trans*-to-*cis* isomerization. When the UV irradiation is ceased, the thermodynamically unfavored *cis* form isomerizes into the stable *trans* form and consequently, the protein crystallites are reassembled. Controlling the isomerization kinetics leads to the production of crystals with different dimensions: while visible light or heat treatment yields crystalline domains with significantly augmented sizes compared to those obtained by direct complexation, spontaneous *cis*-to-*trans* isomerization during the crystallization process produces single crystals with sizes of up to $\approx 50\ \mu m$. We therefore anticipate that this work can be of broad interest in nanofabrication and fundamental studies of optically controlled crystallization.

Results and Discussion

Considering the negatively charged exterior of TMV (pI = 3.9) and ferritin (Ft, pI = 5.4) cages at specific conditions (TMV at pH 5.5 and Ft at pH 7.5), we prepared a cationic azobenzene (*trans*-azoTAB, Figure 1a and S1),[16] and complexed it with the protein cages at corresponding conditions.

An initial study on the structural transition of the azobenzene confirmed the UV-triggered *trans*-to-*cis* isomerization. The system reached a photostationary state (PSS) upon exposure to UV for 1 min, yielding more than 94% *cis*-azoTAB (Figure S2a and Table S1).[15i,17] The stable *trans* form could be restored thermally or under visible-light illumination (Figure S2c–e and Table S1). Under ambient room light, a new PSS with $\approx 68\%$ *trans*-azoTAB was reached in 20 min (half-life: 2 min). Thermal relaxation could yield > 99.9% recovery of *trans*-azoTAB, and the isomerization process was significantly accelerated at elevated temperature: while the required time at 25 °C was 102 h (half-life: 15 h), it was reduced to 27 h at 40 °C (half-life: 2.7 h) and 3 h at 60 °C (half-life: 0.3 h). Alternating exposure to UV and visible light reversibly switched the structural conformation of the azobenzene, and no fatigue was observed for at least 5 cycles (Figure S2f). The *trans*-azoTAB was complexed with the rod-like TMV or the spherical Ft cage in the corresponding buffer (Figure 1a). In the following studies, the protein concentration for both

cages was fixed (4 mg mL^{-1}) while the azobenzene concentration was varied.

The complexation was firstly monitored with dynamic light scattering (DLS) by titrating the cage solutions with *trans*-azoTAB (Figure 1b). No obvious size change in the TMV solution was observed until 6 mM *trans*-azoTAB was added, and the complex size kept increasing with the azobenzene concentration. For Ft, a size increase was observed starting from 3 mM of azobenzene. Selected volume proportions of Ft/*trans*-azoTAB assemblies demonstrated the azobenzene-dependent complex size. However, the titration of Ft with an anionic azobenzene derivative, methyl orange, showed no obvious change in size (Figure S3). TMV and Ft are known to display an anionic exterior at the tested conditions, a property that has been utilized to complex with cationic systems containing multiple charges.[13c,d] In our system, *trans*-azoTAB is mono-charged and has highly hydrophobic aromatic rings. Therefore, both the electrostatic and hydrophobic interactions contribute significantly to complexing the protein cages.[15f]

The pristine cages and the formed assemblies were imaged with different microscopy techniques. In the absence of the cationic azobenzene, TMV and Ft displayed characteristic rod-like and spherical morphologies (Figure S4a and S5a), respectively, and no pronounced aggregation was observed. Needle-like complexes started to emerge in the TMV solution in the presence of 7 mM *trans*-azoTAB that were transformed into thick and long bundles with increasing azobenzene concentration (Figure S4b–e).[13c] On the other hand, irregular complexes were observed when 3 mM *trans*-azoTAB was introduced to the Ft solution (Figure S5b–h), which supported the DLS results. The TMV bundles and Ft complexes were distinguishable under high-magnification electron microscopy (Figure S4f and S5i).

To gain detailed structural information, the cage complexes were subjected to small-angle X-ray scattering (SAXS) measurements. As shown in Figure 1c and d, 2D hexagonally packed lattices were observed with TMV when *trans*-azoTAB concentration reached 7 mM, as indicated by the three main diffraction peaks ($q = 0.0349, 0.0659$, and $0.0746\ \text{Å}^{-1}$, Figure 1c) that correspond to reflections from [10], [11], and [20] planes.[13c,18] A lattice constant of $a = 19.4$ nm was derived from a linear fit of the quadric Miller indices against the measured q values (inset in the bottom panel of Figure 1c), which agrees well with TMV (18.0 nm) being wrapped by an azobenzene layer.[13c] When the *trans*-azoTAB concentration was further increased, the hexagonal arrangement was maintained, but the interparticle spacing was increased, as evidenced by the [10] peak shift to a lower q value (Figure 1c). Such behavior could be attributed to the increased number of azobenzene molecules intercalated between the TMV rods.[18a] In contrast to the previously reported amorphous aggregates obtained with gold nanoparticles,[15e,f] we observed clear diffraction peaks when introducing 4 mM *trans*-azoTAB to the Ft solution (Figure 1d), indicating the formation of 3D-crystalline lattices. The diffraction peak positions ($q = 0.0609, 0.0695$ and $0.0955\ \text{Å}^{-1}$) correspond to reflections from [111], [200], and [220] planes of a face-centered cubic (*fcc*) lattice (bottom
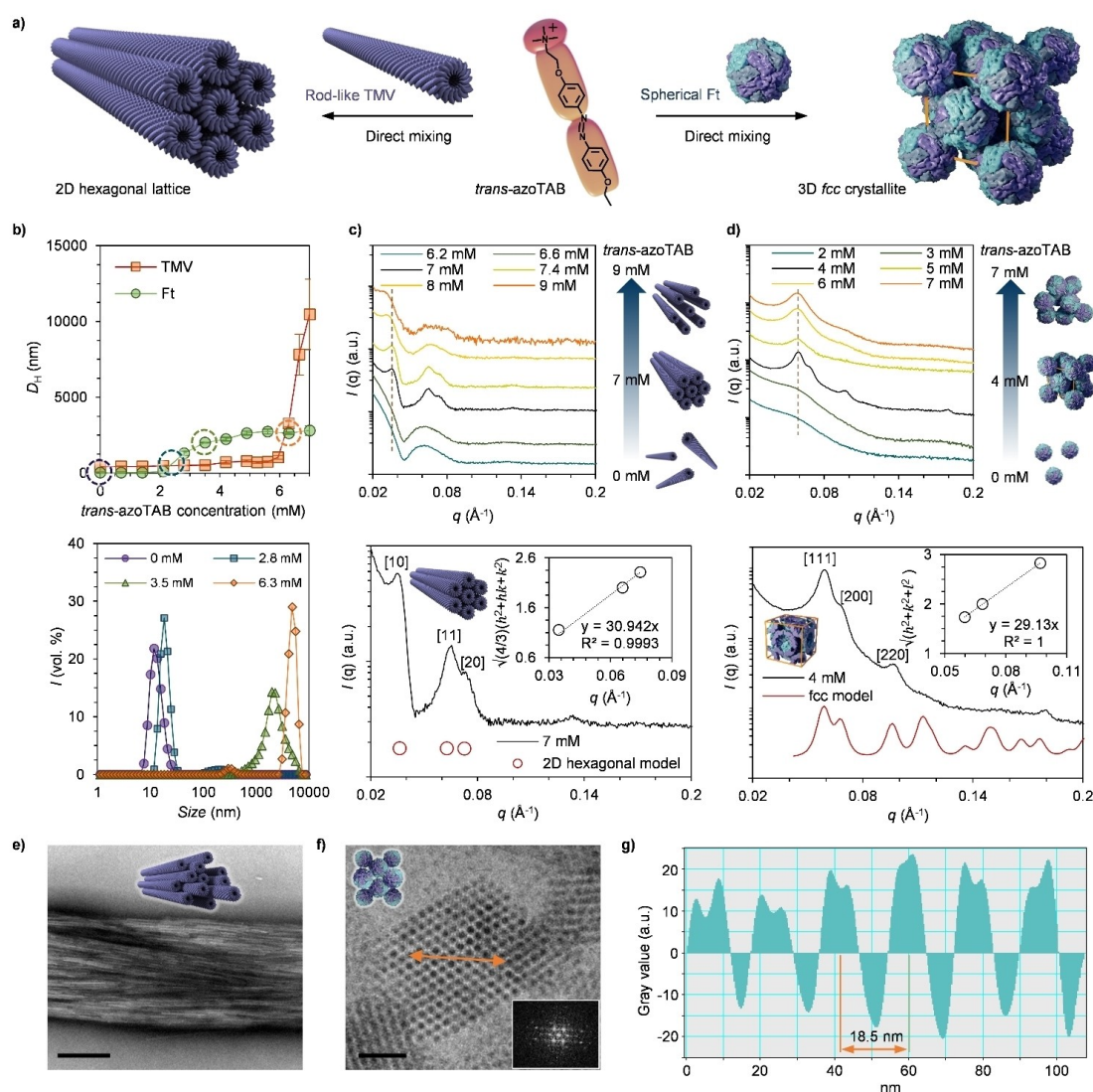
Figure 1. Illustration and characterization of the 2D and 3D crystalline lattices assembled from different protein cages (TMV and Ft) and *trans*-azoTAB through direct mixing. a) Schematic illustration of the 2D hexagonal and 3D *fcc*-packed crystallites formed by directly complexing *trans*-azoTAB with rod-like TMV or spherical Ft. b) Top panel: DLS measurements of the evolution in hydrodynamic diameters of protein cages (4 mg mL^{-1}) titrated with *trans*-azoTAB. Measurements were performed using triplicate samples, and the averaged results with standard deviation are presented. Bottom panel: representative volume proportions of Ft/*trans*-azoTAB assemblies from the top panel as indicated by circles in corresponding colors. c) Top panel: SAXS profiles of TMV/*trans*-azoTAB complexes with varying azobenzene concentrations. As indicated by the schematic illustration, the 2D hexagonal lattice is observed when the azobenzene concentration reaches 7 mM. The *q* value of the first peak is gradually shifted to the lower region as the azobenzene concentration is further increased, demonstrating the increased spacing between TMV nanorods. Bottom panel: comparison between the obtained SAXS data of TMV/*trans*-azoTAB (7 mM) and a model of scattering from a 2D hexagonal structure. Inset: linear fit of the quadric Miller indices as a function of the measured *q*-vector positions yields a lattice constant of $a = 19.4$ nm. d) Top panel: SAXS profiles of Ft/*trans*-azoTAB complexes with varying azobenzene concentrations. As indicated by the schematic presentation, *fcc*-packed crystallites are obtained with 4 mM *trans*-azoTAB, and a further increase in the azobenzene concentration results in amorphous complexes. Bottom panel: comparison between the SAXS data of Ft/*trans*-azoTAB (4 mM) and a model of scattering from an *fcc*-packed lattice. Inset: Linear fit of the quadric Miller indices as a function of the measured *q* values yields a lattice constant of $a = 18.3$ nm. e) TEM image of TMV/*trans*-azoTAB (7 mM). Scale bar: 400 nm. f) Cryo-TEM image of an Ft/*trans*-azoTAB (4 mM) crystallite viewed along the [110] projection axis. Inset indicates the Fast Fourier transform (FFT). Scale bar: 50 nm. g) Integrated profile along the orange line in panel (f), yielding an Ft center-to-center distance of 18.5 nm.

panel, Figure 1d).[6,13a] Plotting the quadric Miller indices against the measured *q* values yielded a lattice constant of $a = 18.3$ nm, and the calculated distance between the two nearest Ft cages was 12.9 nm, agreeing with the Ft diameter (12 nm) separated by the azobenzene.[13a] Unlike the 2D

hexagonal structure, the characteristic diffraction peaks from the *fcc* packing disappeared when the *trans*-azoTAB concentration was above 4 mM (Figure 1d and Figure S5i), indicating disruption of the crystalline lattice.

The crystallites were also directly visualized under transmission electron microscopy (TEM) and cryogenic-TEM (cryo-TEM) (Figure 1e,f). TEM image of TMV/*trans*-azo-TAB (7 mM) revealed the typical parallel alignment of viruses along the fiber axis (Figure 1e),[13c,18b] and the cryo-TEM image of Ft/*trans*-azoTAB (4 mM) clearly showed a crystallite viewed along the [110] projection axis (Figure 1f).[13a] Measuring the dimension of the Ft lattice yielded a lattice constant of 18.5 nm (Figure 1g), which was in good agreement with the data acquired from the SAXS measurements (18.3 nm, Figure 1d).

To confirm the contribution of the electrostatic and hydrophobic interactions, we evaluated the tolerance of the crystallites to electrolytes (NaCl). As shown by DLS measurements (Figure 2a and S6) and optical microscopy images (Figure S7), the sizes of TMV/*trans*-azoTAB (7 mM) and Ft/*trans*-azoTAB (4 mM) were gradually decreased with increasing NaCl concentration, and a plateau was reached at NaCl concentration higher than 240 mM and 400 mM for Ft and TMV, respectively, displaying significant resistance to electrolytes compared to other assemblies mediated by polyelectrolytes.[13a,d,19] The structural integrity of the complexes at varying salt concentrations were monitored with SAXS measurements (Figure 2b,c). It was found that the hexagonal packing of TMV was stable up to 400 mM NaCl (Figure 2b), and the characteristic peaks from the Ft crystallite disappeared in 240 mM NaCl (Figure 2c). Previous work showed that electrostatically driven crystalline structures were normally stable in NaCl up to 100 mM.[13a,d,19] A recent report revealed that the assembly mediated by aromatic stacking interactions exhibited a reverse trend: the reconstituted building blocks were in a dispersed state in the absence of salt, but assembled into arrays in 300 mM NaCl.[10a] The excellent stability of our crystallites against electrolytes confirmed the hypothesis that hydrophobic interactions contributed to the assembly. Moreover, the decrease in size and the disappearance of ordered structures in high salt concentrations suggest that electrostatic interactions also have a major contribution.

Combining the DLS and SAXS results, we can conclude that increasing salt concentration not only screens the interaction between TMV nanorods within the packing, as indicated by the decreasing q values of the [10] peak (Figure 2b), but also gradually unravels TMV bundles into small hexagonal complexes bearing a similar size to single TMV. The hexagonal packing was completely disrupted into free TMV cages when 500 mM NaCl was introduced. On the other hand, the size of the Ft complex was also reduced by NaCl, but the *fcc*-packed arrangement was maintained up to 200 mM NaCl (Figure 2c). At higher NaCl concentrations, amorphous complexes were observed that were eventually disassembled into free Ft particles upon increasing electrolyte concentration.

Upon UV illumination, azobenzene molecules can be switched to the metastable *cis* form, and the solubility in the aqueous phase is also enhanced.[15h,i] Therefore, we anticipate that the protein cage/*trans*-azoTAB complexes can be disassembled by UV light (Figure 3a). As evidenced by DLS measurements (Figure 3b and Figure S8), under UV irradiation (365 nm) the size of the complexes was gradually reduced and eventually reached a similar level as free protein cages, irrespective of the azobenzene concentration. The time required for a full disassembly increased with the azobenzene concentration (Figure 3b and Figure S8f). Microscopy images confirmed the disassembly of the complexes, and high magnification images as well as SAXS measurements unveiled the dispersed state of the cage particles (Figure 3c and Figure S9–S11).

When the UV-disassembled systems were subjected to ambient room light, the cages were reassembled in 1 h and grew into micron-sized assemblies (Figure 3d). Microscopy images and SAXS profiles showed that TMV reassembled into similar bundle structures with the 2D hexagonal arrangement as those obtained upon direct mixing (Figure S12). As for Ft, a particle-like morphology was observed under optical microscopy (Figure 3e and Figure S13), which was in contrast with the irregular complexes obtained by direct mixing Ft and *trans*-azoTAB (Figure S5). The fact
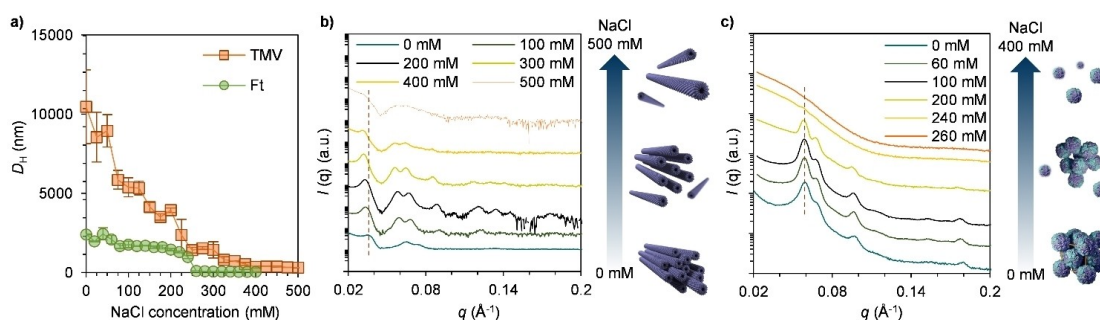
Figure 2. Evaluation of the stability of protein cage/*trans*-azoTAB crystallites in increasing electrolyte concentration. a) Evolution of the hydrodynamic diameters of the crystallites (TMV/*trans*-azoTAB (7 mM) and Ft/*trans*-azoTAB (4 mM)) titrated with NaCl measured with DLS. Measurements were performed using triplicate samples, and the averaged results with standard deviation are presented. b), c) SAXS profiles for b) TMV/*trans*-azoTAB (7 mM) and c) Ft/*trans*-azoTAB (4 mM) in varying NaCl concentrations and the corresponding schematic illustrations on the structural evolution. The hexagonal lattice of TMV/*trans*-azoTAB (7 mM) shows significant resistance to NaCl (up to 400 mM), and the spacing between TMV is increased with increasing salt concentration until full disassembly. The *fcc*-packed crystallite of Ft/*trans*-azoTAB (4 mM) is stable in 200 mM NaCl. At higher concentrations, the lattice is interrupted and eventually disassembled into free particles.
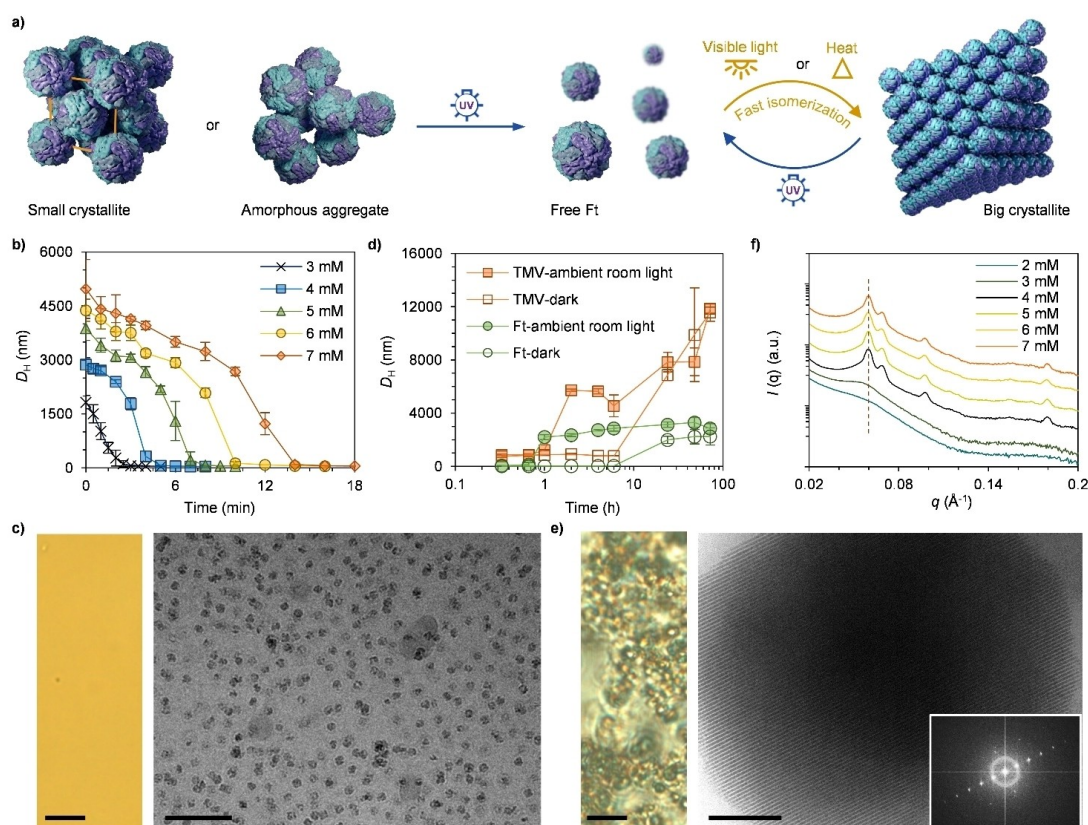
Figure 3. Light-induced structural transition of protein cage/*trans*-azoTAB complexes. a) Schematic illustration of the structural transition of Ft/*trans*-azoTAB complexes upon alternating UV and ambient room light illumination. Alternating UV and ambient room light illumination reversibly switch Ft/*trans*-azoTAB (4 mM) between a dispersed phase and a crystalline state. Moreover, Ft/*trans*-azoTAB crystallites containing higher azobenzene concentrations (5, 6, and 7 mM) are also obtained after a photo-treatment cycle. b) The size evolution of Ft/*trans*-azoTAB with varying azobenzene concentrations under UV illumination measured with DLS. c) Optical microscopy (left) and cryo-TEM (right) images of Ft/*trans*-azoTAB (4 mM) after UV illumination. Scale bar in the optical microscopy image: 10 μm. Scale bar in the cryo-TEM image: 50 nm. d) The reassembly kinetics of UV-disassembled TMV/*trans*-azoTAB (7 mM) and Ft/*trans*-azoTAB (4 mM) under ambient room light or in dark measured with DLS. e) Optical microscopy (left) and cryo-TEM (right) images of the reassembled Ft/*trans*-azoTAB (7 mM) under ambient room light. Inset indicates the FFT. Scale bar in the optical microscopy image: 10 μm. Scale bar in the cryo-TEM image: 200 nm. f) SAXS profiles of Ft/*trans*-azoTAB complexes with varying azobenzene concentrations after one light treatment cycle. DLS measurements were performed using triplicate samples, and the averaged results with standard deviation are presented.
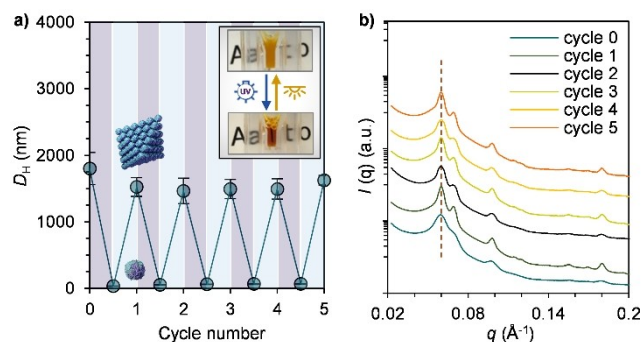
that 32 % of the molecules remain in the *cis* state does not seem to hamper the crystallization. To verify this, we also incubated the UV-disassembled complexes at 60 °C for 3 h to obtain ≈100 % *trans*-azoTAB. Optical microscopy images revealed that Ft/azoTAB (3–7 mM) displayed a similar particle-like structure (Figure S14). Importantly, after the photo or thermal treatment, the SAXS profiles revealed that the *fcc*-packed lattice of Ft/*trans*-azoTAB (4 mM) was recovered (Figure 3f and S15a), and the cryo-TEM images displayed a more ordered crystalline domain (Figure S13f and S15b). The crystallites were also observed in complexes bearing other azobenzene concentrations (Figure 3e,f and S15a).

The reassembly of the cage complexes is attributed to the structural relaxation of *cis*-azoTAB to the more hydrophobic *trans* isomer when subjected to visible light or thermal treatment.[15h,i] The complexes reassembled relatively slowly (hours) compared to those obtained by directly mixing Ft and *trans*-azoTAB (seconds). Therefore, slow

isomerization allows releasing kinetically trapped azobenzene molecules and favors the formation of well-organized structures with long-range order.[20]

We also demonstrated the photo-reversibility of the protein cage crystallites through alternating light illumination. As shown in Figure 4 and Figure S16, DLS measurements showed the reversible switching between micro-sized complexes and nano-sized particles for 5 cycles of alternating photo illumination. The size transition was also visually reflected by the transmittance change of the solutions. Moreover, SAXS results revealed that the crystalline lattices were reliably restored after each ambient room light treatment.
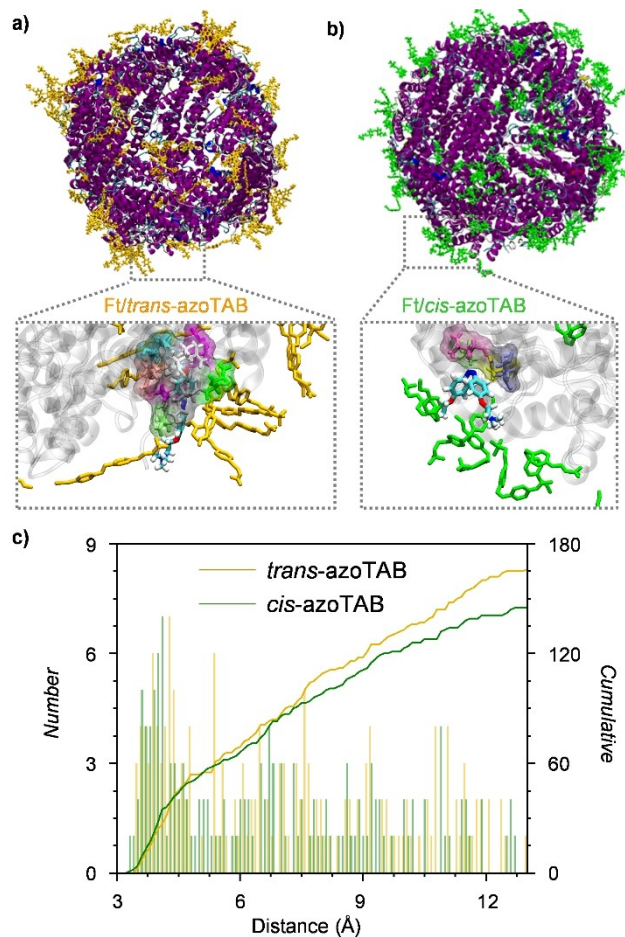
We used all-atom molecular dynamics (AAMD) simulation to investigate the interactions between Ft and *trans*-azoTAB or *cis*-azoTAB.[20] We focused on simulating ferritin-azobenzene and azobenzene-azobenzene interactions. To this end, we simulated one Ft cage in the presence of 1000 *trans*-azoTAB or *cis*-azoTAB molecules and 5000

Angew. Chem. Int. Ed. **2023**, *62*, e202303880 (5 of 9)

© 2023 The Authors. Angewandte Chemie International Edition published by Wiley-VCH GmbH

Figure 4. Reversible photo-controlled switching of Ft/*trans*-azoTAB (4 mM) crystallite. a) The reversible switching in size measured with DLS. In each cycle, the complex is subjected to UV illumination for 10 min, followed by ambient room light exposure for 1 h. The inset image shows the transmittance change upon UV and ambient room light exposure. Measurements were performed using triplicate samples, and the averaged results with standard deviation are presented. b) SAXS profiles of Ft/*trans*-azoTAB (4 mM) show that the *fcc*-packed lattice is reliably reassembled after each light exposure cycle.

Figure 5. AAMD simulation results of the interactions between Ft and *trans*-azoTAB or *cis*-azoTAB. a), b) The orientation and arrangement of a) *trans*-azoTAB (yellow) and b) *cis*-azoTAB (green) on Ft (purple). The bottom panels in both Figures display the zoomed-in area from the top panels, in which the other colors (red, blue, cyan, white, and magenta) indicate the amino acid residues within a distance of 3 Å to the azobenzene molecules. c) The number at a specific distance (column graph) and the cumulative number (curve graph) of $-NC_3H_9^+$ from *trans*-azoTAB and *cis*-azoTAB on Ft. In the range of 0.3–0.7 nm, the cumulative number of $-NC_3H_9^+$ from *trans*-azoTAB and *cis*-azoTAB is similar. Above 0.7 nm, the cumulative number of $-NC_3H_9^+$ from *trans*-azoTAB is ≈15% higher than that from *cis*-azoTAB, indicating a strong interaction between *trans*-azoTAB and protein.

Tris-HCl at pH 7.5 and ran in the isothermal-isobaric (NPT) ensemble for 50 ns. We found that both isomers could bind to the Ft surface and reach an absorption saturation (Figure 5 and S17). Within a distance of 3 Å to the Ft surface, the number of both isomers was similar (≈130). In the longer distance range (between 3 Å and 13 Å), the cumulative number of *trans*-azoTAB was ≈15% higher than that of *cis*-azoTAB, indicating a stronger binding between *trans*-azoTAB and Ft (Figure 5c). It was also found that both isomers were located at the hydrophobic regions of Ft, and the adjacent amino acid residues (<3 Å) included e.g. alanine and leucine (bottom panels in Figure 5a,b). However, the orientation and arrangement of the isomers varied significantly: while *trans*-azoTAB tended to form dimers with $-N(CH_3)_3^+$ groups pointing outward from Ft (Figure 5a), *cis*-azoTAB aggregated into irregular structures, and the orientation of $-N(CH_3)_3^+$ groups was ambiguous (Figure 5b). Analysis of the electrostatic potential on the exterior surface revealed that plain Ft displayed a highly net negative charge (Figure S18). The absorption of the isomers partially neutralized the negative charges, but the protein cages as a whole were still negatively charged (Figure S18).

The free energy was also retrieved to assess the interactions, and the results were summarized in Table S2. The free energy extracted from the interaction between Ft and *trans*-azoTAB (-9.1×10^3 kJ mol^{-1}) was slightly lower than that between Ft and *cis*-azoTAB (-8.2×10^3 kJ mol^{-1}), and the major contribution came from hydrophobic interactions for both isomers (78% for *trans*-azoTAB and 72% for *cis*-azoTAB). These results agreed with the AAMD simulation results that both isomers resided in the hydrophobic regions (Figure 5). Importantly, the free energy extracted from the interaction between *trans*-azoTAB (-286.5×10^3 kJ mol^{-1}) was much lower than that between *cis*-azoTAB (-162.8×10^3 kJ mol^{-1}), indicating a much stronger interaction between *trans*-azoTAB molecules.

It has been reported that the critical micellar concentration of *trans*-azoTAB is ≈10 mM,[17,21] which is more than two times higher than the concentration that induced complex formation in our work. Therefore, combining the experimental and computational data, we propose the following binding mechanism for the cage complex. At low *trans*-azoTAB concentrations (<3 mM), a small portion of the molecules are bound to the cage surface via hydrophobic interaction while the majority are dispersed in the solution. As the concentration is increased, an increasing number of *trans*-azoTAB is attracted to Ft through electrostatic interactions, which significantly reduces the polarity and hence the solubility of *trans*-azoTAB to the aqueous phase. Therefore, Ft particles are assembled by the *trans*-azoTAB

molecules through the combination of hydrophobic and electrostatic interactions. In the presence of electrolytes (NaCl), the hydrophobic interactions between azobenzene are enhanced, generating a multivalency effect that prompts the binding between Ft and azobenzene.[10a, 22] Therefore, the protein cage/*trans*-azoTAB complexes display significant stability against electrolytes compared to other polyelectrolyte-mediated cage assemblies.[13a,d] Upon UV-illumination, *trans*-azoTAB is isomerized to the *cis* form. Therefore, the solubility in the aqueous phase is enhanced, which diminishes the azobenzene-azobenzene interactions, and eventually the cage assemblies.[15h] Following ambient room light treatment, the *trans* isomers and consequently the assembled state is restored.

The spontaneous relaxation kinetics of *cis*-azoTAB at room temperature is significantly slower than the *cis*-to-*trans* isomerization induced by ambient room lighting (Figure S2).[15i] Therefore, we hypothesized that spontaneous *cis*-to-*trans* isomerization could be used to construct large single crystals (Figure 6a). The size evolution was first monitored by DLS measurements at room temperature in dark (Figure 3d). An obvious increase in size was observed with UV-disassembled TMV and Ft complexes in 24 h, a time frame that was much longer than those assembled under ambient room light (1 h). We then used a hanging-drop setup to slowly reassemble the Ft complexes containing varying azobenzene concentrations,[13d] and the solutions were collected and characterized after two weeks of incubation (Figure 6b–d and S19). In the solutions containing more than 2 mM azobenzene, Ft single crystals were observed under an optical microscope with sizes reaching 50 µm. The crystals were also produced with 3 mM azobenzene, a

concentration that did not yield ordered lattices by direct mixing or photo-treatment. The polyhedral crystals were visualized under a scanning electron microscope (SEM), and distinguishable Ft layers were observed in the zoomed-in areas on the crystal surface (Figure 6b–d). SAXS profiles confirmed the *fcc*-packed lattice of the crystals (Figure S19h). In the absence of azoTAB, assembly could be barely observed under the optical microscope. We collected the hanging-drop product of Ft/azoTAB (4 mM). After thoroughly washing with buffer, we used 1 M NaCl to disassemble the product and compared the UV/Vis spectra with that of plain Ft and *trans*-azoTAB (Figure S19i). A clear *trans*-azoTAB peak was observed in the disassembled complex solution. Therefore, it is believed that *trans*-azoTAB plays a key role in mediating the assembly.

We also placed the heat-treated samples (60 °C for 3 h) in the hanging-drop setup for 2 weeks, and optical microscopy images revealed a similar morphology as those only subjected to thermal treatment without the hanging-drop process (Figure S20). Moreover, directly mixing and incubating Ft/*trans*-azoTAB (3–7 mM) for 2 weeks only produced amorphous aggregates (Figure S21). Therefore, it is believed that the large crystals mainly result from the slow *cis*-to-*trans* isomerization and that the tendency for Ft/*trans*-azoTAB to reconfigure into larger crystals is low when *trans*-azoTAB molecules are kinetically trapped. Ft single crystals were also obtained when the UV-disassembled complexes were reassembled in sealed tubes (Figure S22). Therefore, the successful production of Ft single crystals (especially at 3 mM azoTAB) was attributed to the slowed *cis*-to-*trans* isomerization kinetics rather than the increased concentration. With the same setup, similar bundles as those
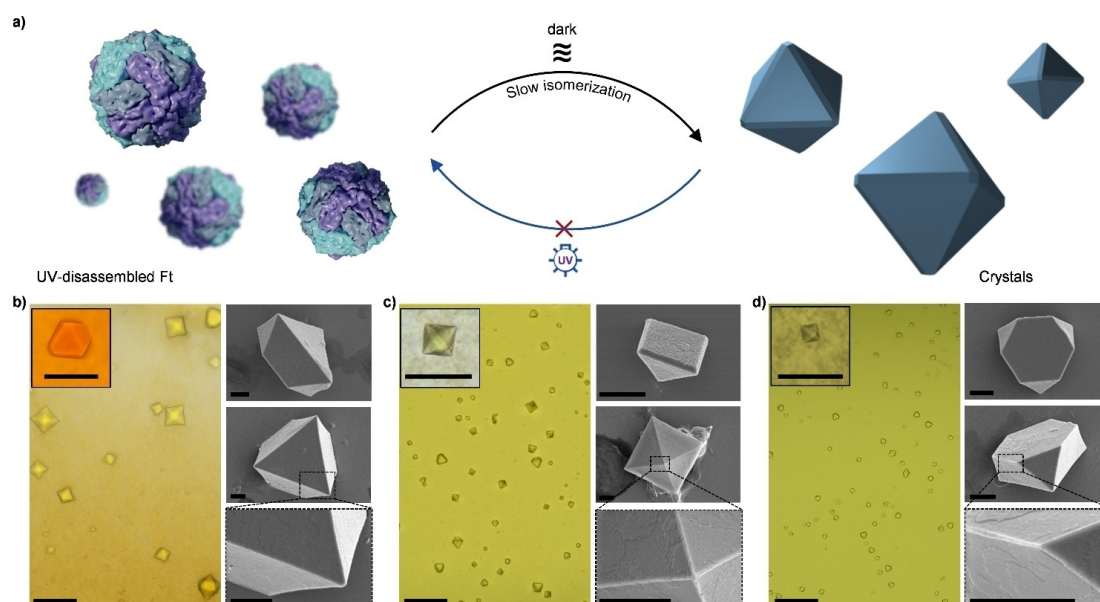
Figure 6. Illustration and characterization of Ft/*trans*-azoTAB crystals assembled via spontaneous structural isomerization of *cis*-azoTAB. a) Schematic illustration of the crystals assembled via slow structural isomerization at room temperature in dark after the UV-induced disassembly. The spontaneously reassembled crystals are stable under UV light. b)–d) Optical microscopy and SEM images of cage crystals containing b) 3 mM, c) 5 mM and d) 7 mM azoTAB. Insets in optical microscopy images show the representative single crystals, and the bottom SEM images in each panel show the zoomed-in area of the middle ones. Scale bar in optical microscopy images: 50 µm. Scale bar in SEM images: 2 µm.

obtained via direct mixing or light treatment were observed with TMV, as revealed by optical microscopy and TEM (Figure S23). We attribute such a phenomenon to the large aspect ratio and higher flexibility of TMV (Figure S4a).

Using spontaneous isomerization is similar to the method that is generally employed to assemble oppositely charged systems into large crystals by carefully adjusting the ionic strength in solutions.[13d,20] Nevertheless, our approach utilizes a non-invasive stimulus (light) and precludes the supply of molecular input (salt), which can be beneficial for the preparation of structures across multiple length scales.[1b] We also synthesized another cationic azobenzene, *trans*-azoFMA (Figure S24), which displayed slower *cis*-to-*trans* isomerization rate (Figure S25) compared to *cis*-azoTAB (Figure S2) in dark. *Trans*-azoFMA exhibited similar performance in complexing Ft and in subsequently triggering the disassembly-reassembly of the complex (Figure S26). Reassembling the UV-disassembled complex (4 mM *trans*-azoFMA) in dark also produced Ft single crystals (Figure S27), demonstrating the versatility of this approach.

The single crystals (Ft/*trans*-azoTAB (3 mM)) were next subjected to UV illumination. Surprisingly, the morphology displayed no apparent degradation even after 24 h UV exposure (Figure S28a–c), showing significantly enhanced stability that was observed with colloidal crystals crosslinked by azobenzene dithiol ligands.[23] In the presence of 200 mM NaCl, the crystals also showed no obvious change for at least 60 min (Figure S28d–f), confirming the excellent stability as revealed by DLS (Figure 2a). However, when irradiated with UV in the presence of 200 mM NaCl, the crystals gradually disappeared in 10 minutes (Figure S28g–l). Therefore, it is believed that at high NaCl concentrations the stability of *trans*-azoTAB-mediated crystals is impaired and additional UV exposure can disassemble the crystals.

Conclusion

In summary, we report a straightforward and robust method for the preparation of protein cage crystals by using a cationic photo-responsive azobenzene. Control over the crystal domain size can be achieved by adjusting the kinetic pathway of the azobenzene: (1) directly complexing Ft with *trans*-azobenzene produces *fcc*-packed crystallites with domains of several hundred nanometers; (2) photo-induced *cis*-to-*trans* isomerization increases the crystal domain size to more than 1 μm; (3) spontaneous *cis*-to-*trans* isomerization, which occurs much more slowly than the respective photoinduced isomerization, of the azobenzene allows growing well-defined crystals with sizes reaching 50 μm. Our method precludes cumbersome preparation procedures or careful regulation of environmental parameters that are common requisites in conventional crystallization approaches. For example, colloidal crystals mediated by DNA hybridization not only require careful sequence design and additional functionalization on the colloidal surface, but it is also essential to fine-tune the environmental temperature to produce large colloidal crystals.[24] Crystal preparation by electrostatic interactions, on the other hand, commonly

involves careful tuning of the electrolyte concentration by e.g. dialysis against water[13a] or electrolyte decomposition.[20] In our method, the initial amorphous or ordered complexes can be readily disintegrated by light, and no molecule or energy input is needed for the construction of large crystals, which simplifies the preparation. We also anticipate that this approach can be extended to other nano-objects, such as inorganic nanoparticles and DNA nanostructures. The non-invasive reversibility and controllability over the periodicity enable fundamental studies of nanostructures and collective behavior. Therefore, this method may find broad application in fabricating metamaterials and studying the associated properties.

Conflict of Interest

The authors declare no conflict of interest.

Data Availability Statement

The data that support the findings of this study are available from the corresponding author upon reasonable request.

Keywords: Azobenzene · Crystallization · Kinetic Pathway · Photo Responsiveness · Protein Cage

[1] a) T. Bian, Z. Chu, R. Klajn, *Adv. Mater.* **2020**, *32*, 1905866; b) W. M. Aumiller, M. Uchida, T. Douglas, *Chem. Soc. Rev.* **2018**, *47*, 3433; c) C. Lv, X. Zhang, Y. Liu, T. Zhang, H. Chen, J. Zang, B. Zheng, G. Zhao, *Chem. Soc. Rev.* **2021**, *50*, 3957; d) J. Zhu, N. Avakyan, A. Kakkis, A. M. Ho, K. Han, Y. Li, Z.

Angew. Chem. Int. Ed. **2023**, *62*, e202303880 (8 of 9)

© 2023 The Authors. Angewandte Chemie International Edition published by Wiley-VCH GmbH

Zhang, T. S. Choi, Y. Na, C. Yu, F. A. Tezcan, *Chem. Rev.* **2021**, *121*, 13701; e) V. Linko, H. Zhang, Nonappa, M. A. Kostiainen, O. Ikkala, *Acc. Chem. Res.* **2022**, *55*, 1785; f) A. Kuzyk, R. Schreiber, Z. Fan, G. Pardatscher, E.-M. Roller, A. Högele, F. C. Simmel, A. O. Govorov, T. Liedl, *Nature* **2012**, *483*, 311.

[2] A. Korpi, E. Anaya-Plaza, S. Välimäki, M. Kostiainen, *Wiley Interdiscip. Rev. Nanomed. Nanobiotechnol.* **2020**, *12*, e1578.

[3] a) J. Sun, C. Dufort, M. Daniel, A. Murali, C. Chen, K. Gopinath, B. Stein, M. De, V. M. Rotello, A. Holzenburg, C. C. Kao, B. Dragnea, *Proc. Natl. Acad. Sci. USA* **2007**, *104*, 1354; b) M. Künzle, T. Eckert, T. Beck, *J. Am. Chem. Soc.* **2016**, *138*, 12731; c) B. D. C. Zeng, G. R. Lázaro, I. B. Tsvetkova, M. F. Hagan, *ACS Nano* **2018**, *12*, 5323.

[4] a) M. Brasch, R. M. Putri, M. V. de Ruiter, D. Luque, M. S. T. Koay, J. R. Castón, J. J. L. M. Cornelissen, *J. Am. Chem. Soc.* **2017**, *139*, 1512; b) S. Sinn, L. Yang, F. Biedermann, D. Wang, C. Kübel, J. J. L. M. Cornelissen, L. D. Cola, *J. Am. Chem. Soc.* **2018**, *140*, 2355; c) T. G. W. Edwardson, S. Tetter, D. Hilvert, *Nat. Commun.* **2020**, *11*, 5410.

[5] a) S. Välimäki, Q. Liu, L. Schoonen, D. F. M. Vervoort, Nonappa, V. Linko, R. J. M. Nolte, J. C. M. van Hest, M. A. Kostiainen, *J. Mater. Chem. B* **2021**, *9*, 1272; b) E. Selivanovitch, M. Uchida, B. Lee, T. Douglas, *ACS Nano* **2021**, *15*, 15687; c) I. Stupka, Y. Azuma, A. P. Biela, M. Imamura, S. Scheuring, E. Pyza, O. Woźnicka, D. P. Maskell, J. G. Heddle, *Sci. Adv.* **2022**, *8*, eabj9424.

[6] S. Chakraborti, A. Korpi, M. Kumar, P. Stępień, M. A. Kostiainen, J. G. Heddle, *Nano Lett.* **2019**, *19*, 3918.

[7] a) A. D. Malay, N. Miyazaki, A. Biela, S. Chakraborti, K. Majsterkiewicz, I. Stupka, C. S. Kaplan, A. Kowalczyk, B. M. A. G. Piette, G. K. A. Hochberg, D. Wu, T. P. Wrobel, A. Fineberg, M. S. Kushwah, M. Kelemen, P. Vavpetič, P. Pelicon, P. Kukura, J. L. P. Benesch, K. Iwasaki, J. G. Heddle, *Nature* **2019**, *569*, 438; b) E. Golub, R. H. Subramanian, J. Esselborn, R. G. Alberstein, J. B. Bailey, J. A. Chiong, X. Yan, T. Booth, T. S. Baker, F. A. Tezcan, *Nature* **2020**, *578*, 172.

[8] a) M. Yang, W. J. Song, *Nat. Commun.* **2019**, *10*, 5549; b) Y. Suzuki, G. Cardone, D. Restrepo, P. D. Zavattieri, T. S. Baker, F. A. Tezcan, *Nature* **2016**, *533*, 369.

[9] a) J. B. Bailey, L. Zhang, J. A. Chiong, S. Ahn, F. A. Tezcan, *J. Am. Chem. Soc.* **2017**, *139*, 8160; b) M. Du, K. Zhou, R. Yu, Y. Zhai, G. Chen, Q. Wang, *Nano Lett.* **2021**, *21*, 1749.

[10] a) K. Zhou, J. Zang, H. Chen, W. Wang, H. Wang, G. Zhao, *ACS Nano* **2018**, *12*, 11323; b) B. Zheng, K. Zhou, T. Zhang, C. Lv, G. Zhao, *Nano Lett.* **2019**, *19*, 4023.

[11] a) K. Zhou, H. Chen, S. Zhang, Y. Wang, G. Zhao, *Chem. Commun.* **2019**, *55*, 7510; b) J. Zhang, X. Wang, K. Zhou, G. Chen, Q. Wang, *ACS Nano* **2018**, *12*, 1673.

[12] K. J. M. Bishop, C. E. Wilmer, S. Soh, B. A. Grzybowski, *Small* **2009**, *5*, 1600.

[13] a) N. K. Beyeh, Nonappa, V. Liljeström, J. Mikkilä, A. Korpi, D. Bochicchio, G. M. Pavan, O. Ikkala, R. H. A. Ras, M. A. Kostiainen, *ACS Nano* **2018**, *12*, 8029; b) M. A. Kostiainen, P. Hiekkataipale, A. Laiho, V. Lemieux, J. Seitsonen, J. Ruokolainen, P. Ceci, *Nat. Nanotechnol.* **2013**, *8*, 52; c) E. Anaya-Plaza, A. Aljarilla, G. Beaune, Nonappa, J. V. I. Timonen, A. de la Escosura, T. Torres, M. A. Kostiainen, *Adv. Mater.* **2019**, *31*, 1902582; d) A. Shaukat, E. Anaya-Plaza, N. K. Beyeh, M. A. Kostiainen, *Chem. Eur. J.* **2022**, *28*, e202104341.

[14] a) M. Weißenfels, J. Gemen, R. Klajn, *Chem* **2021**, *7*, 23; b) G. Ragazzon, L. J. Prins, *Nat. Nanotechnol.* **2018**, *13*, 882; c) S. De, R. Klajn, *Adv. Mater.* **2018**, *30*, 1706750; d) Q. Liu, H. Li, B. Yu, Z. Meng, X. Zhang, J. Li, L. Zheng, *Adv. Funct. Mater.* **2022**, *32*, 2201196.

[15] a) M. A. Kostiainen, P. Ceci, M. Fornara, P. Hiekkataipale, O. Kasyutich, R. J. M. Nolte, J. J. L. M. Cornelissen, R. D. Desautels, J. Van Lierop, *ACS Nano* **2011**, *5*, 6394; b) J. E. Koskela, V. Liljeström, J. Lim, E. E. Simanek, R. H. A. Ras, A. Priimagi, M. A. Kostiainen, *J. Am. Chem. Soc.* **2014**, *136*, 6850; c) M. A. Kostiainen, O. Kasyutich, J. J. L. M. Cornelissen, R. J. M. Nolte, *Nat. Chem.* **2010**, *2*, 394; d) P. K. Kundu, D. Samanta, R. Leizrowice, B. Margulis, H. Zhao, M. Börner, T. Udayabhaskararao, D. Manna, R. Klajn, *Nat. Chem.* **2015**, *7*, 646; e) H. Zhang, J. Muhammad, K. Liu, R. H. A. Ras, O. Ikkala, *Nanoscale* **2019**, *11*, 14118; f) Q. Wang, D. Li, J. Xiao, F. Guo, L. Qi, *Nano Res.* **2019**, *12*, 1563; g) F. J. Rizzuto, C. M. Platnich, X. Luo, Y. Shen, M. D. Dore, C. Lachance-Brais, A. Guarné, G. Cosa, H. F. Sleiman, *Nat. Chem.* **2021**, *13*, 843; h) A.-L. M. Le Ny, C. T. Lee, *J. Am. Chem. Soc.* **2006**, *128*, 6400; i) N. Martin, L. Tian, D. Spencer, A. Coutable-Pennarun, J. L. R. Anderson, S. Mann, *Angew. Chem. Int. Ed.* **2019**, *58*, 14594; j) J. Vialetto, M. Anyfantakis, S. Rudiuk, M. Morel, D. Baigl, *Angew. Chem. Int. Ed.* **2019**, *58*, 9145.

[16] N. Martin, K. P. Sharma, R. L. Harniman, R. M. Richardson, R. J. Hutchings, D. Alibhai, M. Li, S. Mann, *Sci. Rep.* **2017**, *7*, 41327.

[17] A. Diguet, N. K. Mani, M. Geoffroy, M. Sollogoub, D. Baigl, *Chem. Eur. J.* **2010**, *16*, 11890.

[18] a) T. Li, X. Zan, R. E. Winans, Q. Wang, B. Lee, *Angew. Chem. Int. Ed.* **2013**, *52*, 6638; b) V. Liljeström, A. Ora, J. Hassinen, H. T. Rekola, M. Heilala, V. Hynninen, J. J. Joensuu, R. H. A. Ras, P. Törmä, O. Ikkala, M. A. Kostiainen, *Nat. Commun.* **2017**, *8*, 671.

[19] A. Korpi, C. Ma, K. Liu, Nonappa, A. Herrmann, O. Ikkala, M. A. Kostiainen, *ACS Macro Lett.* **2018**, *7*, 318.

[20] T. Bian, A. Gardin, J. Gemen, L. Houben, C. Perego, B. Lee, N. Elad, Z. Chu, G. M. Pavan, R. Klajn, *Nat. Chem.* **2021**, *13*, 940.

[21] M. Geoffroy, D. Faure, R. Oda, D. M. Bassani, D. Baigl, *ChemBioChem* **2008**, *9*, 2382.

[22] M. A. Kostiainen, G. R. Szilvay, J. Lehtinen, D. K. Smith, M. B. Linder, A. Urtti, O. Ikkala, *ACS Nano* **2007**, *1*, 103.

[23] R. Klajn, K. J. M. Bishop, B. A. Grzybowski, *Proc. Natl. Acad. Sci. USA* **2007**, *104*, 10305.

[24] S. Lee, H. A. Calcaterra, S. Lee, W. Hadibrata, B. Lee, E. Oh, K. Aydin, S. C. Glotzer, C. A. Mirkin, *Nature* **2022**, *610*, 674.